

Cite this: *Chem. Sci.*, 2026, 17, 5595

All publication charges for this article have been paid for by the Royal Society of Chemistry

## Selective NH<sub>3</sub>-to-N<sub>2</sub>H<sub>4</sub> conversion electrocatalysed by ruthenium(II)-cymene complexes

Xi Zhang,<sup>a</sup> Shan Zhao,<sup>a</sup> Chen Zhou,<sup>a</sup> Guo Chen,<sup>b</sup> Liru Cao,<sup>c</sup> Jian Lin,<sup>b</sup> Chen Tang,<sup>a</sup> Zhi-Yan Liu,<sup>a</sup> Piao He<sup>a</sup> and Xiao-Yi Yi<sup>\*,a</sup>

A series of ruthenium(II)-cymene complexes [(η<sup>6</sup>-*p*-cymene)Ru(pp)Cl] (1–4) and corresponding NH<sub>3</sub>-ligated complexes [(η<sup>6</sup>-*p*-cymene)Ru(pp)(NH<sub>3</sub>)]PF<sub>6</sub> ([1-NH<sub>3</sub>]PF<sub>6</sub> to [4-NH<sub>3</sub>]PF<sub>6</sub>), where cymene = 4-isopropyltoluene and pp<sup>−</sup> = pyridylpyrrole ligand, have been designed and synthesized. Structural modifications of pp<sup>−</sup> ligands are accomplished through the use of an increasing number of electron-donating methyl groups on the pyrrole unit. Solid-state structural analysis shows that these complexes have a typical piano-stool structure. Electrochemical studies of these complexes illustrate that the introduction of a methyl group to the pp<sup>−</sup> ligand can greatly decrease the oxidation potential of Ru<sup>III/II</sup> from 0.49 V vs. Cp<sub>2</sub>Fe<sup>+0</sup> for [1-NH<sub>3</sub>]PF<sub>6</sub> to 0.16 V vs. Cp<sub>2</sub>Fe<sup>+0</sup> for [4-NH<sub>3</sub>]PF<sub>6</sub>. Controlled potential coulometry experiments show that these complexes exhibit selective catalysis for the oxidation of NH<sub>3</sub> to N<sub>2</sub>H<sub>4</sub> with a turnover number of up to 453.2 at E<sub>app</sub> 0.8 V vs. Cp<sub>2</sub>Fe<sup>+0</sup> for the [4-NH<sub>3</sub>]PF<sub>6</sub> complex. Kinetic and theoretical thermodynamic studies show that the pathway of bimolecular coupling of Ru<sup>II</sup>-aminyl species and the pathway of ammonia nucleophilic attack of Ru<sup>IV</sup>-imide (generated from the disproportionation of Ru<sup>III</sup>-amide) are involved in N–N formation.

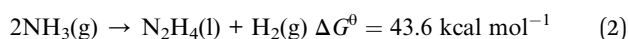
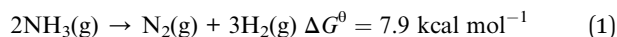
Received 12th November 2025

Accepted 9th January 2026

DOI: 10.1039/d5sc08826g

rsc.li/chemical-science

To meet the challenges of a large-scale energy crisis and environmental pollution, energy-rich H<sub>2</sub> of a green and sustainable nature has attracted much interest as an alternative energy source, although storage and distribution of liquid H<sub>2</sub> still suffer from harsh conditions along with a lack of infrastructure. Ammonia (NH<sub>3</sub>) is a good candidate as a hydrogen energy carrier, and offers approximately 1.7 times the energy density of liquid H<sub>2</sub>.<sup>1–4</sup> The NH<sub>3</sub> industry has not only seen applications worldwide but also has widespread facilities for storage, transport and handing. The classical catalytic cracking reaction for NH<sub>3</sub>-to-H<sub>2</sub> conversion (eqn (1)) requires a precious metal catalyst and high temperature, which are of relatively high cost. Moreover, the generated N<sub>2</sub> product is directly discharged into the air, resulting in low atomic utilization and relatively poor economy in NH<sub>3</sub>-to-H<sub>2</sub> conversion.



Selective electrocatalytic conversion of NH<sub>3</sub> into N<sub>2</sub>H<sub>4</sub> and H<sub>2</sub> (NH<sub>3</sub>-to-N<sub>2</sub>H<sub>4</sub> conversion, eqn (2)) seems more appealing than NH<sub>3</sub>-to-H<sub>2</sub> conversion due to the advantages of not only generating H<sub>2</sub>, but also simultaneously producing high value-added N<sub>2</sub>H<sub>4</sub> (the price of anhydrous hydrazine is about 58 000 USD t<sup>−1</sup>). However, this route is a thermodynamically demanding process (ΔG<sup>0</sup> = 43.6 kcal mol<sup>−1</sup>), and needs to overcome the competitive reaction of spontaneous dehydrogenation of N<sub>2</sub>H<sub>4</sub> to N<sub>2</sub> (eqn (3), ΔG<sup>0</sup> = −35.7 kcal mol<sup>−1</sup>). Hence, highly efficient and selective NH<sub>3</sub>-to-N<sub>2</sub>H<sub>4</sub> conversion is appealing, but remains a huge scientific challenge.<sup>5</sup>

Molecular catalysts can offer several advantages over their heterogeneous counterparts, such as controllable structure, convenient characterization, and well-defined active site nature, which allow for mechanistic studies to elucidate the factors controlling the catalytic activity and selectivity. Since the seminal work by Hamann and Smith III on the electro-oxidation of NH<sub>3</sub> to N<sub>2</sub> catalyzed by [(trpy)(bpy<sup>NMe2</sup>)Ru(NH<sub>3</sub>)](PF<sub>6</sub>)<sub>2</sub> (trpy = 2,2′:6′,2′′-terpyridine, bpy<sup>NMe2</sup> = 4,4′-bis(dimethylamino)-2,2′-bipyridine),<sup>6</sup> significant progress has been made in the development of molecular catalysts for ammonia oxidation.<sup>7–22</sup> Nevertheless, the reported catalytic systems are mostly concerned with the oxidation of NH<sub>3</sub> to N<sub>2</sub>, and there are few reports on the selective catalytic conversion of NH<sub>3</sub> into N<sub>2</sub>H<sub>4</sub>. In 2023, we demonstrated that [Ru(κ<sup>2</sup>-N,N′-

<sup>a</sup>College of Chemistry and Chemical Engineering, Central South University, Changsha, Hunan 410083, P. R. China. E-mail: xyiyi@csu.edu.cn

<sup>b</sup>School of Chemistry and Chemical Engineering, Southwest University, Chongqing, 400715, P. R. China

<sup>c</sup>CAS Key Laboratory of Science and Technology on Applied Catalysis, Dalian Institute of Chemical Physics, Chinese Academy of Sciences, Dalian, 116023, P. R. China



dpp)(bpy)(dmsO)(NH<sub>3</sub>)]PF<sub>6</sub> (Hdpp = 2,5-di(pyridin-2-yl)-1H-pyrrole)<sup>15a</sup> can catalyze the electrocatalytic conversion of NH<sub>3</sub> into N<sub>2</sub>H<sub>4</sub> with unprecedentedly high selectivity (over 97.9%) and turnover frequency (238.9 h<sup>-1</sup>). Although a similar ligated-N<sub>2</sub>H<sub>4</sub> intermediate and a similar N-N formation pathway—such as either bimolecular coupling of a metal-imide<sup>15,18,19,20a</sup> or ammonia nucleophilic attack of a metal-imide<sup>6,10,17,22</sup>—are involved, this catalyst is in sharp contrast with conventional ones that usually generate N<sub>2</sub> as the major N-N coupling product with relatively low turnover frequencies. N<sub>2</sub>H<sub>4</sub>/N<sub>2</sub> selectivity is usually represented by a branch from a ligated-N<sub>2</sub>H<sub>4</sub> intermediate,<sup>14,15a</sup> which could directly release N<sub>2</sub>H<sub>4</sub> or continue to be over-oxidized to release N<sub>2</sub>. The release of N<sub>2</sub>H<sub>4</sub> from a ligated-N<sub>2</sub>H<sub>4</sub> intermediate to restart the catalytic cycle is one of the key issues for the selective oxidation of NH<sub>3</sub> to N<sub>2</sub>H<sub>4</sub>. Thus, rational design of the ancillary ligand backbone is still a desirable strategy for developing highly efficient and selective catalysts for NH<sub>3</sub>-to-N<sub>2</sub>H<sub>4</sub> conversion.

We have long been interested in the study of metal complexes based on the pyridylpyrrole (pp<sup>-</sup>) ligand, which is structurally analogous to bipyridine.<sup>23</sup> Notwithstanding the similar structure and coordination properties, the π-donation from the pyrrolyl group in the pp<sup>-</sup> ligand increases the energy of the metal-based LUMO in the M-N<sub>2</sub>H<sub>4</sub> intermediate, thus weakening the M-N<sub>2</sub>H<sub>4</sub> bond and facilitating the release of N<sub>2</sub>H<sub>4</sub>.<sup>24</sup> In addition, the negative charge of the pyrrolyl unit not only lowers the overpotential of the metal complex but also reduces the overall positive charge of the reactive intermediate, which is a major cause of instability in the intermediates during the AO catalytic cycle.<sup>23</sup> Herein, we design an ancillary pp<sup>-</sup> ligand using an increasing number of electron-donating methyl groups on the pyrrole unit to regulate the electronic structure of

the metal complex. Corresponding ruthenium(II)-cymene complexes [(η<sup>6</sup>-*p*-cymene)Ru(pp)Cl] (where pp<sup>-</sup> is HL1 = 2-(1H-pyrrol-2-yl)pyridine (1), HL2 = 2-(4-methyl-1H-pyrrol-2-yl)pyridine (2), HL3 = 2-(3,5-dimethyl-1H-pyrrol-2-yl)pyridine (3), and HL4 = 2-(3,4,5-trimethyl-1H-pyrrol-2-yl)pyridine (4)) and corresponding NH<sub>3</sub>-ligated complexes [(η<sup>6</sup>-*p*-cymene)Ru(pp)(NH<sub>3</sub>)]PF<sub>6</sub> ([1-NH<sub>3</sub>]<sup>+</sup>PF<sub>6</sub><sup>-</sup> to [4-NH<sub>3</sub>]<sup>+</sup>PF<sub>6</sub><sup>-</sup>) are reported. Their selective catalysis for NH<sub>3</sub>-to-N<sub>2</sub>H<sub>4</sub> conversion and the catalytic mechanism are also presented.

As shown in Fig. 1a, complexes 1–4 are synthesized by treatment of dimeric precursor of [(η<sup>6</sup>-*p*-cymene)RuCl<sub>2</sub>]<sub>2</sub> and a deprotonated pyridylpyrrole ligand in CH<sub>2</sub>Cl<sub>2</sub> at 0 °C in moderate yield (~50%). The corresponding NH<sub>3</sub>-ligated complexes [(η<sup>6</sup>-*p*-cymene)Ru(pp)(NH<sub>3</sub>)]PF<sub>6</sub> ([1-NH<sub>3</sub>]<sup>+</sup>PF<sub>6</sub><sup>-</sup> to [4-NH<sub>3</sub>]<sup>+</sup>PF<sub>6</sub><sup>-</sup>) are synthesized in over 60% yield by treatment of 1–4 with one equiv. of AgPF<sub>6</sub> in CH<sub>3</sub>CN followed by bubbling NH<sub>3</sub> gas. These complexes are stable in common organic solvents, and are fully characterized by ESI-MS, NMR and IR spectroscopy (Fig. S6–S29). Compared to 1–4, the <sup>1</sup>H NMR spectra of [1-NH<sub>3</sub>]<sup>+</sup>PF<sub>6</sub><sup>-</sup> to [4-NH<sub>3</sub>]<sup>+</sup>PF<sub>6</sub><sup>-</sup> show a newly added broad single peak at ~2.0 ppm due to the ligated-NH<sub>3</sub>. Similarly, the IR spectra of [1-NH<sub>3</sub>]<sup>+</sup>PF<sub>6</sub><sup>-</sup> to [4-NH<sub>3</sub>]<sup>+</sup>PF<sub>6</sub><sup>-</sup> show an additional band at ~3340–3350 cm<sup>-1</sup> due to N–H stretching, also indicating that NH<sub>3</sub> binds to the Ru center. The solid-state structures of 1–4 and [2-NH<sub>3</sub>]<sup>+</sup>PF<sub>6</sub><sup>-</sup> are shown in Fig. 1b. The crystallographic data and selected bond distances and angles are listed in Tables S1–S6. These complexes exhibit a typical piano-stool structure with one pp<sup>-</sup>, one cymene and one Cl<sup>-</sup> (or NH<sub>3</sub>) ligand coordinating to the ruthenium center. The bond distance of Ru–N<sub>pyrrole</sub> (2.042(10)–2.074(3) Å) is slightly shorter than that of Ru–N<sub>pyridine</sub> (2.101(2)–2.113(3) Å), mainly due to the electrostatic interaction between the Ru atom and the anionic pyrrolide N atom. In [2-

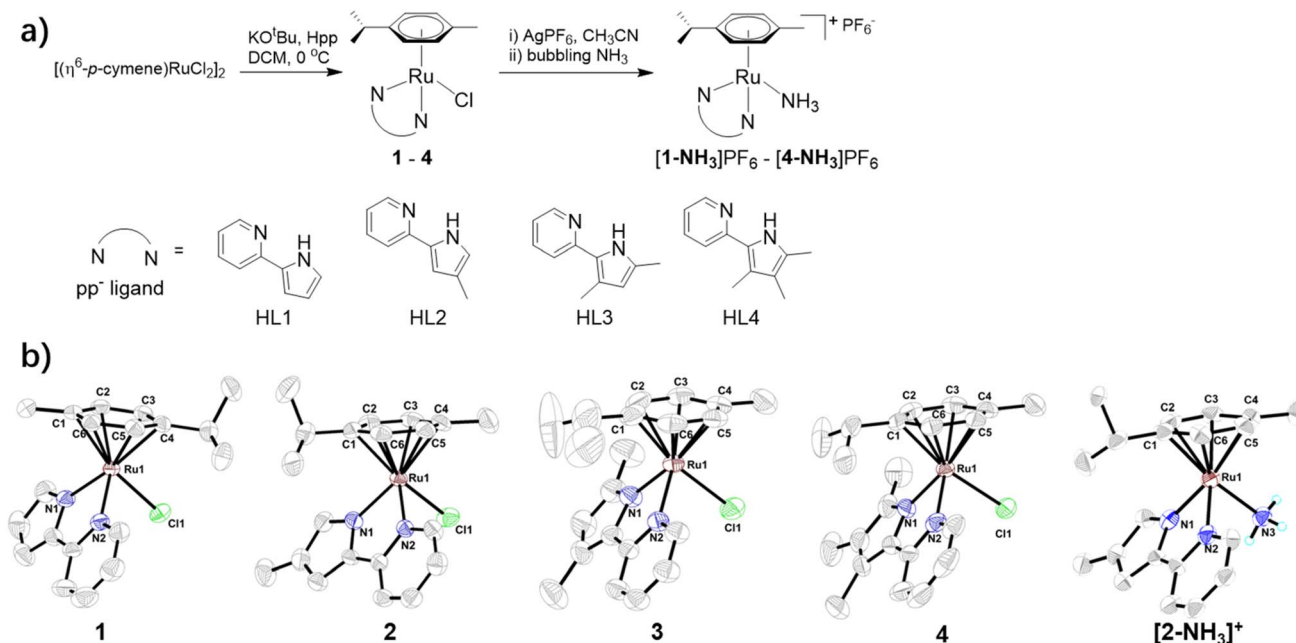


Fig. 1 (a) The synthetic routes of 1–4, and [1-NH<sub>3</sub>]<sup>+</sup>PF<sub>6</sub><sup>-</sup> to [4-NH<sub>3</sub>]<sup>+</sup>PF<sub>6</sub><sup>-</sup>. (b) Solid-state structures of complexes 1–4 and [2-NH<sub>3</sub>]<sup>+</sup>. The hydrogen atoms on cymene, the pp<sup>-</sup> ligand and anionic PF<sub>6</sub><sup>-</sup> in [2-NH<sub>3</sub>]<sup>+</sup>PF<sub>6</sub><sup>-</sup> are omitted for clarity.



$\text{NH}_3\text{]}PF_6$ ,  $\text{NH}_3$  coordinates to the Ru center with a Ru–N bond distance of 2.138(12) Å, which is similar to that of other  $\text{NH}_3$ -ligated Ru(II) complexes.

The electrochemical behavior of the title complexes in  $\text{CH}_3\text{CN}$  is investigated by cyclic voltammetry (CV) and differential pulse voltammetry (DPV) using a  $\text{AgCl/Ag}$  electrode in a saturated KCl solution as a reference electrode. Unless otherwise specified, all potentials are converted into  $E_{1/2}$  vs.  $\text{Cp}_2\text{Fe}^{+/0}$  in  $\text{CH}_3\text{CN}$  by adding  $-0.43$  V to the measured potential.

The electrochemical behavior of **1–4** is shown in Fig. 2a. The first oxidation wave is assigned to ruthenium center oxidation ( $\text{Ru}^{\text{II}} \rightarrow \text{Ru}^{\text{III}}$ ). The electro-donating nature of the  $\text{pp}^-$  ligand significantly influences the redox potential of these complexes, leading to a decreasing  $\text{Ru}^{\text{III/II}}$  reduction potential from 0.37 V for **1** to 0.04 V for **4** with an increase in the number of electron-donating methyl groups on the pyrrole unit. The redox potentials of the second oxidation wave at  $\sim 1.2$  V and third oxidation wave at  $\sim 1.6$  V (see the DPV curves in Fig. 2a) are independent of the methyl substituted  $\text{pp}^-$  ligand. These could clearly be assigned to  $\text{Cl}^-$  and cymene ligand oxidation events, respectively.<sup>25,26</sup> Fig. 2b shows that  $[\mathbf{1-NH}_3]\text{PF}_6$  to  $[\mathbf{4-NH}_3]\text{PF}_6$  exhibit two oxidation waves. The first one (0.49 V, 0.36 V, 0.23 V and 0.16 V for  $[\mathbf{1-NH}_3]\text{PF}_6$  to  $[\mathbf{4-NH}_3]\text{PF}_6$ , respectively) is attributed to their metal center oxidation from  $\text{Ru}^{\text{II}}$  to  $\text{Ru}^{\text{III}}$ . Compared to **1–4**, the  $\text{Ru}^{\text{III/II}}$  redox potentials of  $[\mathbf{1-NH}_3]\text{PF}_6$  to  $[\mathbf{3-NH}_3]\text{PF}_6$  are anodically shifted by  $\sim 0.12$  V, mainly due to the  $\pi$ -donating capability of the  $\text{Cl}^-$  ligand in the former. Upon expanding the voltage window, unlike the second oxidation peak corresponding to  $\text{Ru}^{\text{IV/III}}$  reported in our previous literature,<sup>15</sup> these complexes exhibited no additional metal-centered oxidation waves except for the second oxidation peak assigned to cymene

ligand oxidation at  $\sim 1.6$  V.<sup>26</sup> However, a weak new wave marked by a rhombus appears at 0.75–0.88 V when scanning in the cathodic direction (Fig. 2c). This suggests that a disproportionation of  $\text{Ru}^{\text{III}}$  species possibly occurs to give  $\text{Ru}^{\text{II}}$  and  $\text{Ru}^{\text{IV}}$  species, and then  $\text{Ru}^{\text{IV}}$  is reduced to  $\text{Ru}^{\text{III}}$  on the reverse scan. Taking  $[\mathbf{1-NH}_3]\text{PF}_6$  as an example, its  $\text{Ru}^{\text{III}}$  intermediate formed by  $1e^-$  oxidation is proposed to undergo rapid disproportionation to  $\text{Ru}^{\text{II}}[\mathbf{1-NH}_3]^+$  and a  $\text{Ru}^{\text{IV}}$  imido intermediate and simultaneously reach equilibrium. Thus, the wave at 0.88 V on the reverse scan can be assigned to the reduction of  $\text{Ru}^{\text{IV}}$  species to  $\text{Ru}^{\text{III}}$  species of  $[\mathbf{1-NH}_3]^+$ . To further confirm the  $1e^-$  oxidation to form a  $\text{Ru}^{\text{III}}$  intermediate, CV was employed, with ferrocene added as the internal reference at an equimolar concentration to  $[\mathbf{1-NH}_3]^+$ . As shown in Fig. S30, the diffusion coefficient of complex  $[\mathbf{1-NH}_3]^+$  ( $1.58 \times 10^{-5} \text{ cm}^2 \text{ s}^{-1}$ ) is very close to that of ferrocene ( $1.37 \times 10^{-5} \text{ cm}^2 \text{ s}^{-1}$ ), and the peak areas of  $[\mathbf{1-NH}_3]^+$  and ferrocene are almost the same in their respective CV plots, preliminarily indicating that the first oxidation wave of  $[\mathbf{1-NH}_3]^+$  involved only one electron transfer. The more critical evidence in the reversible charge transfer process is the slope analysis of  $E$  vs.  $\lg[(I_1 - I)/I]$  (where  $E$  is the potential and  $I_1$  is the limiting current).<sup>27</sup> As shown in Fig. S31, a linear relationship was observed between  $E$  and  $\lg[(I_p - I)/I]$  (where  $I_p$  is the peak current, used in place of  $I_1$  due to the irreversible oxidation wave of  $[\mathbf{1-NH}_3]^+$ ), with a slope  $m = 2.3RT/nF$  (where  $R$  is the ideal gas constant,  $T = 298.15$  K, and  $F = 96485 \text{ C mol}^{-1}$ ). The fitted slope from the experimental data was 0.84, yielding an electron transfer number  $n \approx 0.84$ . These results collectively confirm that only a single electron transfer occurs at the electrode surface, followed by a redox disproportionation chemical step.

The electrochemical behavior of  $[\mathbf{1-NH}_3]\text{PF}_6$  to  $[\mathbf{4-NH}_3]\text{PF}_6$  in the presence of 0.05 M  $\text{NH}_3$  is shown in Fig. 3. Complexes  $[\mathbf{1-}$

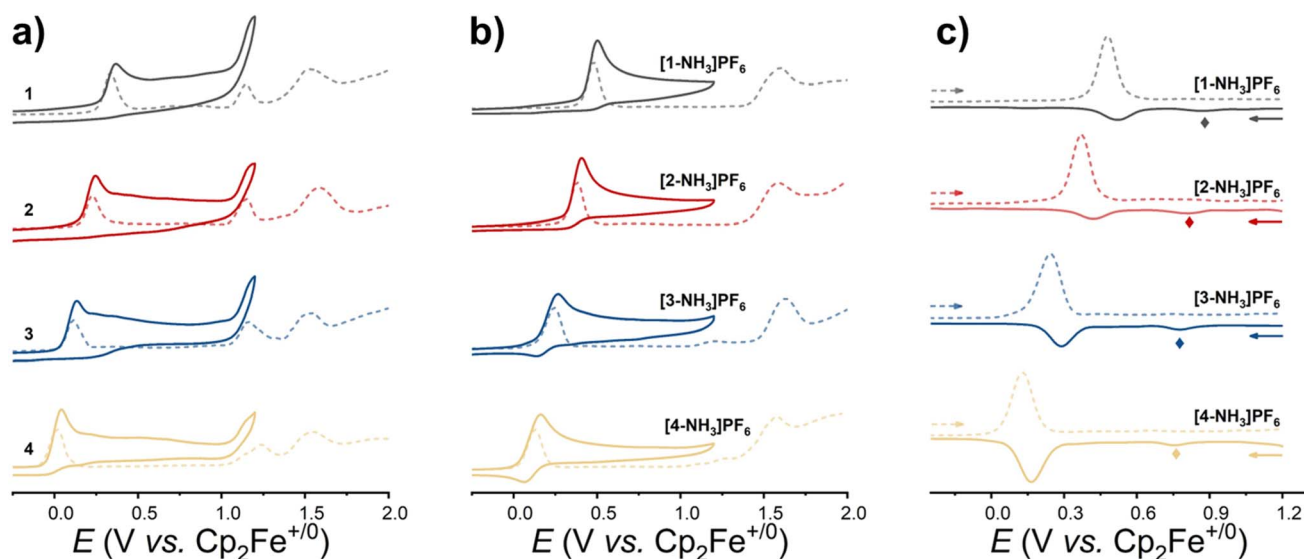


Fig. 2 Electrochemical behavior of the title complexes in  $\text{CH}_3\text{CN}$  solution. (a) CV (solid lines) and DPV (dotted lines) plots of **1–4**; (b) CV (solid lines) and DPV (dotted lines) plots of  $[\mathbf{1-NH}_3]\text{PF}_6$  to  $[\mathbf{4-NH}_3]\text{PF}_6$ ; and (c) DPV plots of  $[\mathbf{1-NH}_3]\text{PF}_6$  to  $[\mathbf{4-NH}_3]\text{PF}_6$  in the anodic direction (dotted lines) and cathodic direction (solid lines). Conditions:  $[\text{Ru}] = 1$  mM, scan rate  $0.1 \text{ V s}^{-1}$  for CV and  $0.008 \text{ V s}^{-1}$  for DPV, 0.1 M  $\text{Bu}_4\text{NPF}_6$  as the supporting electrolyte, glassy carbon as the working electrode, platinum wire as the counter electrode,  $\text{AgCl/Ag}$  in saturated KCl aqueous solution as the reference electrode.



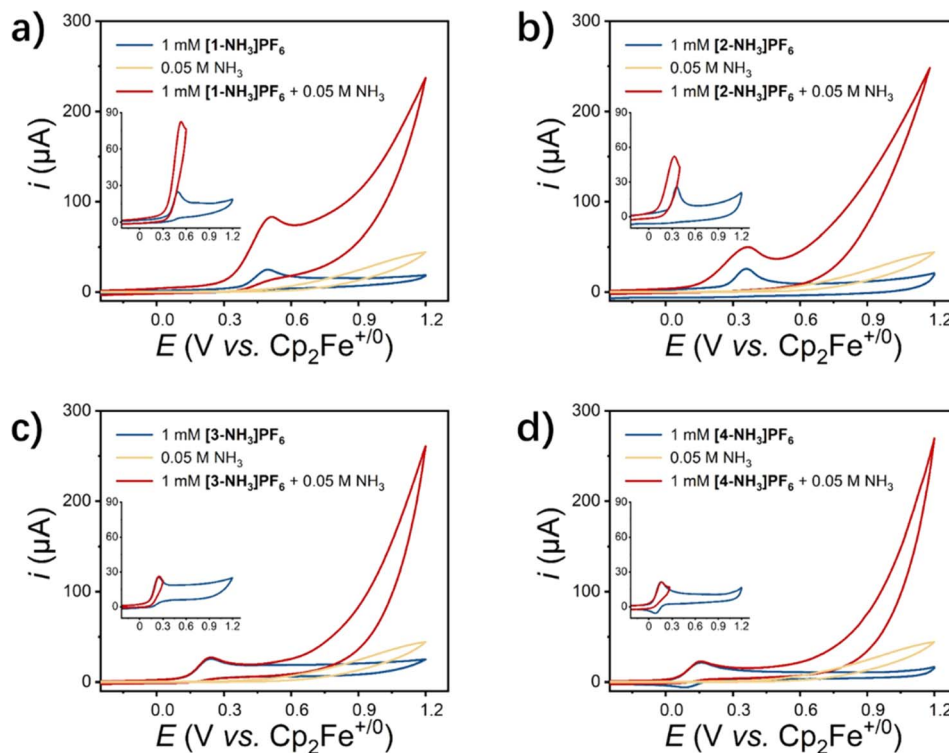


Fig. 3 CV plots of (a) [1-NH<sub>3</sub>]**PF<sub>6</sub>**, (b) [2-NH<sub>3</sub>]**PF<sub>6</sub>**, (c) [3-NH<sub>3</sub>]**PF<sub>6</sub>** and (d) [4-NH<sub>3</sub>]**PF<sub>6</sub>** solution with/without 0.05 M NH<sub>3</sub>/NH<sub>4</sub>PF<sub>6</sub> in CH<sub>3</sub>CN. Conditions: [Ru] = 1 mM, scan rate 0.1 V s<sup>-1</sup>, 0.1 M Bu<sub>4</sub>NPF<sub>6</sub> as the supporting electrolyte, glassy carbon as the working electrode, platinum wire as the counter electrode, AgCl/Ag in saturated KCl aqueous solution as the reference electrode. Insets: CVs. in the voltage window of -0.25–1.2 V.

NH<sub>3</sub>]**PF<sub>6</sub>** and [2-NH<sub>3</sub>]**PF<sub>6</sub>** display a slightly increased catalytic current ( $i_{\text{cat}}$ ) over Ru<sup>III</sup> species with low onset potentials of 0.15 V and 0.10 V, respectively (inset figures of Fig. 3). Although Ru<sup>IV</sup> species of the title complexes are not clearly observed in the CV studies, the catalytic current increases sharply at potentials over 0.6 V. For complexes [3-NH<sub>3</sub>]**PF<sub>6</sub>** and [4-NH<sub>3</sub>]**PF<sub>6</sub>**, a catalytic current only appears at a high potential, and there is no catalytic current over Ru<sup>III</sup> species. Anodic currents ( $i_p$ ) of the Ru<sup>III/IV</sup> redox couple and the catalytic current of [1-NH<sub>3</sub>]**PF<sub>6</sub>** to [4-NH<sub>3</sub>]**PF<sub>6</sub>** in the presence of 0.05 M NH<sub>3</sub> increase linearly with the square root of the scan rate (Fig. S33), indicating diffusion-controlled behavior of these ruthenium catalysts under test conditions. The rate constant ( $k_{\text{cat}}$ ) and maximum turnover frequency (TOF<sub>max</sub>) of [1-NH<sub>3</sub>]**PF<sub>6</sub>** to [4-NH<sub>3</sub>]**PF<sub>6</sub>** for ammonia oxidation are estimated. The diffusion coefficients ( $D_{\text{Ru}}$ ) and rate constants ( $k_{\text{cat}}$ ) of [1-NH<sub>3</sub>]**PF<sub>6</sub>** to [4-NH<sub>3</sub>]**PF<sub>6</sub>** are  $1.58 \times 10^{-5}$  cm<sup>2</sup> s<sup>-1</sup>,  $1.71 \times 10^{-5}$  cm<sup>2</sup> s<sup>-1</sup>,  $1.82 \times 10^{-5}$  cm<sup>2</sup> s<sup>-1</sup>, and  $1.94 \times 10^{-5}$  cm<sup>2</sup> s<sup>-1</sup>; and 4.5 s<sup>-1</sup>, 4.9 s<sup>-1</sup>, 5.2 s<sup>-1</sup>, and 5.4 s<sup>-1</sup>, respectively, which are determined from the dependence of  $i_p$  and  $\nu^{1/2}$  based on the Randles-Sevcik relation (eqn (4)) and linear fitting of  $i_{\text{cat}}/i_p$  with  $\nu^{-1/2}$  based on eqn (5), respectively. The TOF<sub>max</sub> values at a scan rate of 0.1 V s<sup>-1</sup> based on eqn (6) are estimated to be  $4.92 \times 10^{-2}$  s<sup>-1</sup>,  $5.48 \times 10^{-2}$  s<sup>-1</sup>,  $5.81 \times 10^{-2}$  s<sup>-1</sup>, and  $6.29 \times 10^{-2}$  s<sup>-1</sup>.

$$i_p = 0.446nFAC_{\text{cat}}\sqrt{(nFvD_{\text{Ru}})/(RT)} \quad (4)$$

$$i_{\text{cat}}/i_p = 2.242n_{\text{cat}}\sqrt{(k_{\text{cat}}RT)/(nFv)} \quad (5)$$

$$\text{TOF}_{\text{max}} = 0.1992\left(\frac{Fv}{RT}\right)\left(\frac{n^3}{n_p^2}\right)\left(\frac{i_{\text{cat}}}{i_p}\right)^2 \quad (6)$$

To confirm the electrocatalysis of [1-NH<sub>3</sub>]**PF<sub>6</sub>** to [4-NH<sub>3</sub>]**PF<sub>6</sub>** for NH<sub>3</sub>-to-N<sub>2</sub>H<sub>4</sub> conversion, controlled potential coulometry (CPC) experiments are conducted in a conventional sealed three-electrode cell with 2.0 M NH<sub>3</sub>, 0.01 mM catalyst and 0.1 M [n-Bu<sub>4</sub>N]**PF<sub>6</sub>** electrolyte in dried CH<sub>3</sub>CN under an Ar atmosphere. Carbon cloth (1 cm<sup>2</sup>), a Pt plate (1 cm<sup>2</sup>) and Ag/AgCl in saturated KCl aqueous solution are used as the working electrode, counter electrode and reference electrode, respectively. Possible gas products (such as N<sub>2</sub>, H<sub>2</sub>) are determined by the GC method (Fig. S1). Possible products in the electrolyte (such as N<sub>2</sub>H<sub>4</sub>, NO<sub>2</sub><sup>-</sup>, NO<sub>3</sub><sup>-</sup>) are quantitatively analyzed *via* chemical methods (Fig. S2–S5).<sup>28–30</sup>

To obtain general information for the CPC experiments, first, control experiments are employed. As shown in Table S7, only negligible N<sub>2</sub>H<sub>4</sub> and N<sub>2</sub> are generated at low applied potential (such as  $E_{\text{app}}$  0.39 V) for 24 h. However, 21.6 μmol of N<sub>2</sub>H<sub>4</sub> and 0.5 μmol of N<sub>2</sub> are produced at  $E_{\text{app}}$  0.8 V for 2 h, indicating that the bare electrode causes slow ammonia oxidation at relatively high potential. Subsequently, the complex [2-NH<sub>3</sub>]**PF<sub>6</sub>** is chosen to investigate the relationship between catalytic performance over time and applied potential (Table 1 and Fig. S38, S39,



Table 1 The electrocatalytic performances of [1-NH<sub>3</sub>]<sub>3</sub>PF<sub>6</sub> to [4-NH<sub>3</sub>]<sub>3</sub>PF<sub>6</sub> in CH<sub>3</sub>CN<sup>a</sup>

Entry	Cat	[NH <sub>3</sub> ] (M)	<i>E</i> <sub>app</sub>	Time (h)	TON <sub>H<sub>2</sub></sub> / <i>n</i> <sub>H<sub>2</sub></sub> (μmol)	TOF <sub>H<sub>2</sub></sub> (h <sup>-1</sup> )	TON <sub>N<sub>2</sub>H<sub>4</sub></sub> / <i>n</i> <sub>N<sub>2</sub>H<sub>4</sub></sub> (μmol)	TOF <sub>N<sub>2</sub>H<sub>4</sub></sub> (h <sup>-1</sup> )	TON <sub>N<sub>2</sub></sub> / <i>n</i> <sub>N<sub>2</sub></sub> (μmol)	TOF <sub>N<sub>2</sub></sub> (h <sup>-1</sup> )	FE <sub>N<sub>2</sub>H<sub>4</sub></sub> <sup>b</sup> (%)	S <sub>N<sub>2</sub>H<sub>4</sub></sub> <sup>c</sup> (%)
1	[1-NH <sub>3</sub> ] <sub>3</sub> PF <sub>6</sub>	2.0	0.39	24	17.2 13.7	0.7	16.5 13.2	0.7	Trace	—	86.3	100
2	[2-NH <sub>3</sub> ] <sub>3</sub> PF <sub>6</sub>	2.0	0.26	24	11.5 9.2	0.5	11.0 8.8	0.5	Trace	—	89.7	100
3	[3-NH <sub>3</sub> ] <sub>3</sub> PF <sub>6</sub>	2.0	0.13	24	Trace	—	Trace	—	Trace	—	—	—
4	[4-NH <sub>3</sub> ] <sub>3</sub> PF <sub>6</sub>	2.0	0.06	24	Trace	—	Trace	—	Trace	—	—	—
5	[1-NH <sub>3</sub> ] <sub>3</sub> PF <sub>6</sub>	2.0	0.8	2	377.3 301.9	188.7	356.2 284.9	178.1	5.3 4.2	2.7	88.2	98.6
6	[2-NH <sub>3</sub> ] <sub>3</sub> PF <sub>6</sub>	2.0	0.8	2	403.5 322.8	201.8	393.9 315.2	197.0	2.2 1.8	1.1	90.8	99.4
7	[3-NH <sub>3</sub> ] <sub>3</sub> PF <sub>6</sub>	2.0	0.8	2	430.1 344.1	215.1	418.2 334.5	209.1	4.3 3.4	2.2	93.5	99.0
8	[4-NH <sub>3</sub> ] <sub>3</sub> PF <sub>6</sub>	2.0	0.8	2	461.6 369.3	230.8	453.2 362.5	230.8	2.4 1.9	1.2	91.9	99.5
9	[4-NH <sub>3</sub> ] <sub>3</sub> PF <sub>6</sub>	0.05	0.8	2	156.6 125.3	78.3	151.0 120.8	75.5	1.5 1.2	0.8	87.6	99.0
10	5 (ref. 15a)	2.0	1.0	24	5870 2348	244.6	5735 2293.8	238.9	43.9 17.56	1.8	36.6	97.8
11	6 (ref. 15b)	2.0	1.0	2	801.5 561.1	400.8	721.5 505.1	360.8	13.7 9.6	6.9	99.2	98.1
12	7 (ref. 15c)	2.0	1.0	2	844.2 616.2	422.1	786.8 566.4	393.4	19.8 14.3	9.9	99.3	93.1

<sup>a</sup> Conditions: carbon cloth (1 cm<sup>2</sup>) as the working electrode, a platinum plate (1 cm<sup>2</sup>) as the counter electrode, AgCl/Ag in saturated KCl aqueous solution as the reference electrode, [cat] = 0.01 mM. The background is subtracted to obtain the number of moles of the products H<sub>2</sub>, N<sub>2</sub> and N<sub>2</sub>H<sub>4</sub>.

<sup>b</sup> FE<sub>N<sub>2</sub>H<sub>4</sub></sub> = 2 *n*<sub>N<sub>2</sub>H<sub>4</sub></sub>*F*/*it* × 100%. <sup>c</sup> S<sub>N<sub>2</sub>H<sub>4</sub></sub> = *n*<sub>N<sub>2</sub>H<sub>4</sub></sub>/(*n*<sub>N<sub>2</sub></sub> + *n*<sub>N<sub>2</sub>H<sub>4</sub></sub>) × 100%.

Tables S8, S9). The amounts of N<sub>2</sub>H<sub>4</sub> as an absolutely dominant anodic product and H<sub>2</sub> as a cathodic product increase with an increase of the applied potential from 0.2 V to 1.0 V (Fig. S38). Other anode products of NO<sub>2</sub><sup>-</sup> and NO<sub>3</sub><sup>-</sup> are not determined due to the absence of oxygen sources in the catalytic system. Holding the applied potential at 0.8 V, the generation of N<sub>2</sub>H<sub>4</sub> and H<sub>2</sub> keeps increasing over time, however, the turnover frequency (TOF) and Faraday efficiency (FE) of N<sub>2</sub>H<sub>4</sub> formation continuously decrease (Fig. S39 and Table S9). The loss of TOF and FE for long-term electrolysis might be caused by over-oxidation of the produced H<sub>2</sub> in the sealed CPC cell. A decrease in *i*<sub>cat</sub> under a H<sub>2</sub> atmosphere indicating the current consumption of H<sub>2</sub> oxidation cannot be ignored (Fig. S40). The *i*<sub>cat</sub> remains almost unchanged after 100 consecutive CV cycles or electrolysis for 2 h, indicating that these Ru catalysts under catalytic conditions have satisfactory stability (Fig. S41 and S42). A thoroughly rinsed electrode after catalysis shows no ruthenium deposition and no catalytic activity, indicating solution-based electrocatalysis (Fig. S43–S45 and Table S7). Notably, N<sub>2</sub>H<sub>4</sub> is prone to undergo either catalytic oxidation or disproportionation decomposition to yield N<sub>2</sub>. In contrast, complexes [1-NH<sub>3</sub>]<sub>3</sub>PF<sub>6</sub>–[4-NH<sub>3</sub>]<sub>3</sub>PF<sub>6</sub> exhibit good selectivity toward N<sub>2</sub>H<sub>4</sub> formation. CV measurements of [1-NH<sub>3</sub>]<sub>3</sub>PF<sub>6</sub> in MeCN containing N<sub>2</sub>H<sub>4</sub> confirm that they are inactive toward N<sub>2</sub>H<sub>4</sub> oxidation (Fig. S54).

To clarify the catalytic performance of the catalysts at the initial stage of Ru<sup>III</sup> species formation, we selected a potential 0.1 V lower than the Ru<sup>III/II</sup> potential of the catalysts (0.39 V for [1-

NH<sub>3</sub>]<sub>3</sub>PF<sub>6</sub>, 0.26 V for [2-NH<sub>3</sub>]<sub>3</sub>PF<sub>6</sub>, 0.13 V for [3-NH<sub>3</sub>]<sub>3</sub>PF<sub>6</sub>, and 0.06 V for [4-NH<sub>3</sub>]<sub>3</sub>PF<sub>6</sub>) as the applied potential in the CPC experiment. N<sub>2</sub>H<sub>4</sub> and almost equiv. molar of H<sub>2</sub> are produced in the [1-NH<sub>3</sub>]<sub>3</sub>PF<sub>6</sub> and [2-NH<sub>3</sub>]<sub>3</sub>PF<sub>6</sub> catalyst systems, and the generation of N<sub>2</sub> could be negligible (entries 1 and 2). From comparison to the result of the control CPC experiments at *E*<sub>app</sub> 0.39 V, this indicates that the catalytic activity originates from the catalyst but not the bare electrode. The catalytic conversion of NH<sub>3</sub> to N<sub>2</sub>H<sub>4</sub> achieves ~100% selectivity. This behavior also aligns with our earlier ruthenium catalysts containing pyridylpyrrole operated at low applied potentials *via* bimolecular N–N coupling of Ru<sup>III</sup>-amide to form N<sub>2</sub>H<sub>4</sub>.<sup>15,18,19,20a</sup> As expected in the CV studies, no ammonia oxidation products (N<sub>2</sub>H<sub>4</sub> or N<sub>2</sub>) are generated in the [3-NH<sub>3</sub>]<sub>3</sub>PF<sub>6</sub> and [4-NH<sub>3</sub>]<sub>3</sub>PF<sub>6</sub> catalyst systems, only over Ru<sup>III</sup> species at low potential (entries 3 and 4). Next, we carried out CPC experiments at higher applied potential *E*<sub>app</sub> of 0.80 V. Correspondingly, the catalytic efficiency of [1-NH<sub>3</sub>]<sub>3</sub>PF<sub>6</sub> to [4-NH<sub>3</sub>]<sub>3</sub>PF<sub>6</sub> significantly increased. As shown in Table 1, entries 5–8, N<sub>2</sub>H<sub>4</sub> is still determined as the dominant anodic product with a yield range from 284.9 μmol to 362.5 μmol. The turnover frequency (TOF) of N<sub>2</sub>H<sub>4</sub> formation reaches 178.1 h<sup>-1</sup> for [1-NH<sub>3</sub>]<sub>3</sub>PF<sub>6</sub>, 197.0 h<sup>-1</sup> for [2-NH<sub>3</sub>]<sub>3</sub>PF<sub>6</sub>, 209.1 h<sup>-1</sup> for [3-NH<sub>3</sub>]<sub>3</sub>PF<sub>6</sub> and 226.6 h<sup>-1</sup> for [4-NH<sub>3</sub>]<sub>3</sub>PF<sub>6</sub>. The selectivity and Faraday efficiency based on N<sub>2</sub>H<sub>4</sub> formation are over 98.6% and 88.2%, respectively. In this work, [4-NH<sub>3</sub>]<sub>3</sub>PF<sub>6</sub> also shows excellent selectivity and high catalytic activity for the oxidation of low-concentration NH<sub>3</sub> to generate N<sub>2</sub>H<sub>4</sub>. We carried out CPC experiments in a low-concentration NH<sub>3</sub> solution (0.05 M) at the



same potential. After 2 h, catalytic amounts of  $\text{H}_2$  (125.3  $\mu\text{mol}$ ),  $\text{N}_2\text{H}_4$  (120.8  $\mu\text{mol}$ ) and  $\text{N}_2$  (1.2  $\mu\text{mol}$ ) were generated. This result breaks through the limitation of conventional catalytic systems that rely on high ammonia concentrations to achieve high selectivity (entry 9).

The CV and CPC experiments illustrate that complexes  $[\mathbf{1-NH}_3]\text{PF}_6$  and  $[\mathbf{2-NH}_3]\text{PF}_6$  for  $\text{Ru}^{\text{III}}$  species and  $[\mathbf{1-NH}_3]\text{PF}_6$  to  $[\mathbf{4-NH}_3]\text{PF}_6$  for  $\text{Ru}^{\text{IV}}$  species readily undergo ammonia oxidation to generate  $\text{N}_2\text{H}_4$ . To explore the detailed mechanism of these complexes, we carried out theoretical calculations on the activation energy of each step in the catalytic procedure for the  $[\mathbf{1-NH}_3]\text{PF}_6$  and  $[\mathbf{4-NH}_3]\text{PF}_6$  catalysts. A summary of the proposed mechanism and alternative pathway is shown in Fig. 4.

As shown in Fig. 4a, complexes  $[\mathbf{1-NH}_3]^+$  and  $[\mathbf{4-NH}_3]^+$  are first oxidized to  $\text{Ru}^{\text{III}}$ -amide  ${}^2[\mathbf{1-I}]^+$  and  ${}^2[\mathbf{4-I}]^+$  (the left superscript shows the spin state) *via* a  $1e^-/\text{H}^+$  transfer process with  $\Delta G$  of 8.0 and 6.3  $\text{kcal mol}^{-1}$ , respectively. Spin density distribution calculations (Fig. S55) reveal that the spin densities of  ${}^2[\mathbf{1-I}]^+$  and  ${}^2[\mathbf{4-I}]^+$  are primarily located on the Ru center (0.50 and 0.47  $e^-$ ) and N atom of  $\text{NH}_2$  (0.50 and 0.50  $e^-$ ), indicating that the  $\text{Ru}^{\text{III}}$ -amide species has  $\text{Ru}^{\text{II}}$ -aminyl character *via* interconversion of  $\text{Ru}^{\text{III}}-\text{NH}_2^- \rightleftharpoons \text{Ru}^{\text{II}}-\text{NH}_2\text{O}^\bullet$ . The  $\text{Ru}^{\text{II}}$ -aminyl species is an active intermediate and can readily generate  $\text{N}_2\text{H}_4$  *via* a bimolecular  $\text{Ru}^{\text{II}}-\text{NH}_2^-$  coupling reaction.<sup>15,18,19,20a</sup> For the  $[\mathbf{1-NH}_3]\text{PF}_6$  catalyst, theoretical calculations elucidate the coupling process between two  ${}^2[\mathbf{1-I}]^+$  molecules, which proceeds

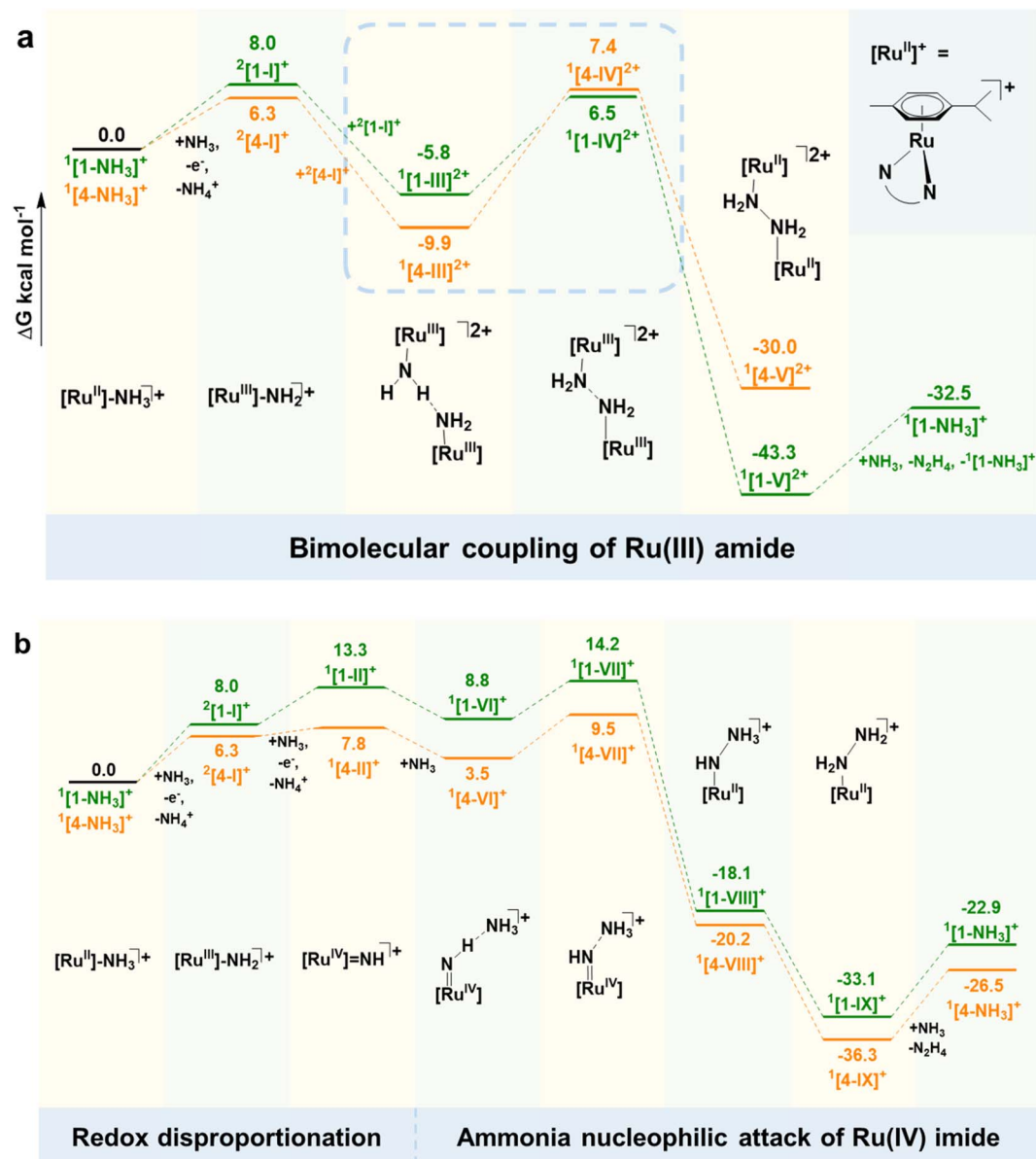


Fig. 4 Calculated pathways of ammonia oxidation catalysed by  $[\mathbf{1-NH}_3]\text{PF}_6$  and  $[\mathbf{4-NH}_3]\text{PF}_6$ , where the free energy changes ( $\Delta G$ ) of individual steps for  $[\mathbf{1-NH}_3]\text{PF}_6$  and  $[\mathbf{4-NH}_3]\text{PF}_6$  are presented in green and orange, respectively. (a) At low potential, hydrazine formation *via* bimolecular coupling of  $\text{Ru}^{\text{III}}$  amide; (b) at high potential, hydrazine generation through ammonia nucleophilic attack of  $\text{Ru}^{\text{IV}}$  imide *via* redox disproportionation.  $[\text{Ru}^{\text{II}}]^+ = [(\eta^6\text{-}p\text{-cymene})\text{Ru}(\text{pp})]^+$ .  $\Delta G$  is calculated relative to  $\text{Cp}_2\text{Fe}^{+/0}$ , with values given in  $\text{kcal mol}^{-1}$ .



through transition states  $^1[1-III]^{2+}$  and  $^1[1-IV]^{2+}$  to ultimately form the thermodynamically stable hydrazine-bridged bimetallic complex  $^1[1-V]^{2+}$ . The catalytic cycle is completed by a mildly endothermic hydrazine dissociation process, with an overall energy barrier of  $12.3 \text{ kcal mol}^{-1}$ .

This bimolecular coupling pathway is supported by the CPC experiment of  $[1-NH_3]PF_6$  at low applied potential (0.39 V), where only  $N_2H_4$  as an ammonia oxidation product is observed. In addition, its catalytic current over  $Ru^{III}$  species is independent of the increase of  $[NH_3]$  (10–50 mM), also indicating that ammonia seems not to be involved in  $N_2H_4$  formation (Fig. S35) only over  $Ru^{III}$  species. A similar bimolecular coupling pathway to form  $N_2H_4$  over  $Ru^{III}$  species is observed in our reported ruthenium catalysts,<sup>15</sup> and has recently been confirmed in the  $[(trpy)(bpy^{NMe_2})Ru(NH_3)](PF_6)_2$  catalyst system.<sup>14</sup> Interestingly, in the bimolecular coupling pathway, the energy barrier for the conversion of  $^1[4-III]^{2+}$  to  $^1[4-V]^{2+}$  ( $17.3 \text{ kcal mol}^{-1}$ ) is only  $5 \text{ kcal mol}^{-1}$  higher than that for  $^1[1-III]^{2+}$  to  $^1[1-V]^{2+}$ . However, CV and CPC studies on the structurally analogous complex  $[4-NH_3]PF_6$  demonstrate that its  $Ru^{III}$  species ( $^2[4-I]^+$ ) cannot trigger ammonia oxidation. This suggests that the difference in energy barrier does not play a decisive role in determining whether N–N bond formation occurs. From a kinetic perspective, an increased number of methyl groups (three methyl groups in  $[4-NH_3]PF_6$ ) enhances steric hindrance, which disfavors the bimolecular coupling pathway and appears to be the dominant controlling factor.

Following the  $1e^-/H^+$  transfer process, the subsequent second  $1e^-/H^+$  oxidation to form  $Ru^{IV}$ -imide species  $^1[1-II]^+$  and  $^1[4-II]^+$  is less endergonic with  $\Delta G$  of 5.3 and  $1.5 \text{ kcal mol}^{-1}$ , respectively. Compared to the first oxidation step, the significantly reduced  $\Delta G$  values indicate thermodynamically more favorable formation of  $Ru^{IV}$ -imide species. Analysis of the combined free energy changes reveals that the redox disproportionation of  $Ru^{III}$ -amide to generate  $Ru^{II}$ -ammine and  $Ru^{IV}$ -imide exhibits  $\Delta G$  values of  $-2.7$  and  $-4.8 \text{ kcal mol}^{-1}$ , respectively, demonstrating a highly spontaneous thermodynamic process. Therefore, the redox disproportionation pathway to form  $Ru^{IV}$ -imide species is thermodynamically preferred over direct oxidation of  $Ru^{III}$ -amide, explaining the absence of an observable  $Ru^{IV/III}$  redox couple under CV test conditions. Notably, the redox disproportionation of  $^2[4-I]^+$  seems to be more favorable than that of  $^2[1-I]^+$ , which is less exergonic. Subsequently, the  $Ru^{IV}$ -imide species  $^1[1-II]^+$  and  $^1[4-II]^+$  initiate ammonia oxidation *via* nucleophilic attack pathways. First,  $^1[1-II]^+$  and  $^1[4-II]^+$  readily interact with  $NH_3$  to generate  $^1[1-VI]^+$  and  $^1[4-VI]^+$  intermediates ( $\Delta G = -4.5$  and  $-4.3 \text{ kcal mol}^{-1}$ , respectively) due to the formation of a hydrogen bond between the H atom of the imide and the N atom of the approaching  $NH_3$ . Subsequently, terminal  $N_2H_4$ -ligated  $^1[1-IX]^+$  and  $^1[4-IX]^+$  are formed through transition states  $^1[1-VII]^+$  and  $^1[4-VII]^+$  ( $\Delta G^\ddagger = 5.4$  and  $6.0 \text{ kcal mol}^{-1}$ , respectively) and intermediates  $^1[1-VIII]^+$  and  $^1[4-VIII]^+$ . The formation of  $^1[1-IX]^+$  and  $^1[4-IX]^+$   $N_2H_4$ -ligated intermediates through the reaction of ammonia and  $Ru^{IV}$ -imides  $^1[1-II]^+$  and  $^1[4-II]^+$  is highly exergonic by 46.4 and  $44.1 \text{ kcal mol}^{-1}$ , respectively. Finally, the catalytic cycle is restarted by endergonic evolution of  $N_2H_4$  through  $N_2H_4$ -by-

$NH_3$  substitution of  $^1[1-IX]^+$  and  $^1[4-IX]^+$  ( $\Delta G = 10.2$  and  $9.8 \text{ kcal mol}^{-1}$ , respectively). Unlike other ruthenium molecular catalysts only generating  $N_2$  as the N–N coupling product, the  $\pi$ -donor capability of the pyrrolyl group of the ancillary  $pp^-$  ligand in the title complexes helps to release  $N_2H_4$  through  $N_2H_4$ -by- $NH_3$  substitution of the  $N_2H_4$ -ligated intermediate, thus hindering  $N_2H_4$  overoxidation to generate  $N_2$ .<sup>24</sup>

The kinetic studies of the title complexes also support an ammonia nucleophilic attack route over  $Ru^{IV}$ -imide species. As shown in Fig. S35 and S36, the catalytic current  $i_{cat}$  (at  $E = 1.2 \text{ V}$ ) linearly increases with the increase of  $[NH_3]$  (0.010–0.050 M) and  $[cat]$  (0.2–1.0 mM), clearly indicating that there is a single-site molecular catalytic pathway. Notably, unlike  $i_{cat}$  at 0.05 M  $NH_3$  showing a linear relationship with  $\nu^{1/2}$ , the  $i_{cat}$  at 1.0 M  $NH_3$  almost does not change with increasing scan rate, indicating that the  $i_{cat}$  is no longer determined by the bulk diffusion of catalyst or  $NH_3$  but by the rate of regeneration of active  $Ru^{IV}$ -imide species at the electrode.<sup>11</sup> This seems to confirm that when ammonia is present in high concentrations, redox disproportionation to generate  $Ru^{IV}$ -imide could be the slow step, and the nucleophilic coupling pathway could prevail, which is consistent with the recent results of mechanism studies of the  $[(trpy)(bpy^{NMe_2})Ru(NH_3)](PF_6)_2$  catalyst system.<sup>14</sup>

In summary, a series of ruthenium(II)-cymene  $NH_3$ -ligated complexes are synthesized and fully characterized. By regulating the electronic structure of the ancillary ligand, the oxidation potential of the ruthenium center is gradually reduced from 0.49 V for  $[1-NH_3]PF_6$  to 0.16 V for  $[4-NH_3]PF_6$ . Unlike the structurally analogous half-sandwich ferric catalyst  $[Cp^*Fe(1,2-Ph_2PC_6H_4NH)(NH_3)]^+$  containing a phosphinoamido ligand to only generate  $N_2H_4$  stoichiometrically,<sup>17</sup>  $[1-NH_3]PF_6$  to  $[4-NH_3]PF_6$  exhibit good performance for the selective electrocatalytic conversion of  $NH_3$  to  $N_2H_4$  with at least 98.6% selectivity and 86.3% Faraday efficiency. The mechanism studies illustrate that the  $Ru^{III}$ -amide intermediate has radical  $Ru^{II}$ -aminyl character *via* the inter-conversion  $Ru^{III}-NH_2 \rightleftharpoons Ru^{II}-NH_2\dot{\square}$ . Bimolecular coupling of the  $Ru^{II}$ -aminyl species readily generates a  $N_2H_4$ -bridged biruthenium intermediate in  $[1-NH_3]PF_6$  and  $[2-NH_3]PF_6$  catalyst systems, but not in  $[3-NH_3]PF_6$  and  $[4-NH_3]PF_6$  catalyst systems. Another pathway of  $N_2H_4$  formation in  $[1-NH_3]PF_6$  and  $[4-NH_3]PF_6$ , the nucleophilic attack of  $Ru^{IV}$ -imide species by ammonia, is more feasible due to lower energy barriers of  $5.4 \text{ kcal mol}^{-1}$  and  $6.0 \text{ kcal mol}^{-1}$ , compared to the bimolecular coupling pathway with energy barriers of  $12.3$  and  $17.3 \text{ kcal mol}^{-1}$ , respectively. This single-site molecular catalytic pathway is supported by a linear relationship between the catalytic current and concentration of catalyst and ammonia.

## Author contributions

Xiao-Yi Yi as the corresponding author contributed to project design and paper revision. Xi Zhang mainly contributed to synthesis and electrocatalysis studies of the titled complexes, writing the preliminary draft. Shan Zhao and Guo Chen contributed to the assist with synthesis. Contribution of Liru Cao and Jian Lin lied in assisting with project design. Zhi-Yan



Liu contributed to supplement data during the paper revision process. Piao He contributed to the DFT calculations.

## Conflicts of interest

The authors declare no competing financial interest.

## Data availability

The raw data including synthesis, characterization, and photophysical and catalytic properties of these complexes are available from the corresponding author, upon reasonable request.

CCDC 1 (2320736), 2 (2324232), 3 (2321021), 4 (2321506) and [2-NH<sub>3</sub>]PF<sub>6</sub> (2427138) contain the supplementary crystallographic data for this paper.

The authors confirm that the data supporting the findings of this study are available within the article and/or its supplementary information (SI). Supplementary information: general methods for synthesis and characterization, crystallographic refinement, cyclic voltammetry experiments and electrolysis experiments, and DFT calculations. See DOI: <https://doi.org/10.1039/d5sc08826g>.

## Acknowledgements

This work was supported by the National Natural Science Foundation of China (22471291) and the Foundation of Central South University Research Programme of Advanced Interdisciplinary (2023QYJC019) and Key Program of Hunan Provincial Natural Science Foundation of China (2025JJ30006).

## References

- (a) H. Tan, Z. Sang, Y. Tian, W. Peng, X. Liu and J. Liang, Ammonia as a Green Carbon-Free Fuel: A Pathway to the Sustainable Energy Economy, *ACS Energy Lett.*, 2024, **9**, 5120–5136; (b) D. T. Tran, T. H. Nguyen, H. Jeong, P. K. L. Tran, D. Malhotra, K. U. Jeong, N. H. Kim and J. H. Lee, Recent Engineering Advances in Nanocatalysts for NH<sub>3</sub>-to-H<sub>2</sub> Conversion Technologies, *Nano Energy*, 2022, **94**, 106929.
- S. A. Lee, M. G. Lee and H. W. Jang, Catalysts for Electrochemical Ammonia Oxidation: Trend, Challenge, and Promise, *Sci. China Mater.*, 2022, **65**, 3334–3352.
- L. Jiang and X. Fu, An Ammonia-Hydrogen Energy Roadmap for Carbon Neutrality: Opportunity and Challenges in China, *Engineering*, 2021, **7**, 1688–1691.
- N. M. Adli, H. Zhang, S. Mukherjee and G. Wu, Review—Ammonia Oxidation Electrocatalysis for Hydrogen Generation and Fuel Cells, *J. Electrochem. Soc.*, 2018, **165**, J3130–J3147.
- (a) J. Li, F. Zhang, H. Xiong, Y. Cai and B. Zhang, Molecular Catalysts for Electrocatalytic Ammonia Oxidation, *Sci. China Chem.*, 2024, **67**, 3976–3993; (b) D. N. Stephens and M. T. Mock, Molecular Complexes for Catalytic Ammonia Oxidation to Dinitrogen and the Cleavage of N-H Bonds, *Eur. J. Inorg. Chem.*, 2024, e202400039; (c) H. Y. Liu, H. M. C. Lant, C. C. Cody, J. Jelusic, R. H. Crabtree and G. W. Brudvig, Electrochemical Ammonia Oxidation with Molecular Catalysts, *ACS Catal.*, 2023, **13**, 4675–4682.
- F. Habibzadeh, S. L. Miller, T. W. Hamann and M. R. Smith, Homogeneous Electrocatalytic Oxidation of Ammonia to N<sub>2</sub> under Mild Conditions, *Proc. Natl. Acad. Sci. U. S. A.*, 2019, **116**, 2849–2853.
- K. Nakajima, H. Toda, K. Sakata and Y. Nishibayashi, Ruthenium-catalysed oxidative conversion of ammonia into dinitrogen, *Nat. Chem.*, 2019, **11**, 702–709.
- P. L. Dunn, S. I. Johnson, W. Kaminsky and R. M. Bullock, Diversion of Catalytic C-N Bond Formation to Catalytic Oxidation of NH<sub>3</sub> through Modification of the Hydrogen Atom Abstractor, *J. Am. Chem. Soc.*, 2020, **142**, 3361–3365.
- J. Holub, N. Vereshchuk, F. J. Sanchez-Baygual, M. Gil-Sepulcre, J. Benet-Buchholz and A. Llobet, Synthesis, Structure, and Ammonia Oxidation Catalytic Activity of Ru-NH<sub>3</sub> Complexes Containing Multidentate Polypyridyl Ligands, *Inorg. Chem.*, 2021, **60**, 13929–13940.
- M. J. Trenerry, C. M. Wallen, T. R. Brown, S. V. Park and J. F. Berry, Spontaneous N<sub>2</sub> formation by a diruthenium complex enables electrocatalytic and aerobic oxidation of ammonia, *Nat. Chem.*, 2021, **13**, 1221–1227.
- S. I. Jacob, A. Chakraborty, A. Chamas, R. Bock, L. Sepunaru and G. Ménard, Rapid Aqueous Ammonia Oxidation to N<sub>2</sub> Using a Molecular Ru Electrocatalyst, *ACS Energy Lett.*, 2023, **8**, 3760–3766.
- A. M. Beiler, A. Denisiuk, J. Holub, F. J. Sánchez-Baygual, M. Gil-Sepulcre, M. Z. Ertem, D. Moonshiram, A. Piccioni and A. Llobet, Heterogeneous Electrochemical Ammonia Oxidation with a Ru-bda Oligomer Anchored on Graphitic Electrodes via CH- $\pi$  Interactions, *ACS Energy Lett.*, 2023, **8**, 172–178.
- S. Feng, J. Chen, R. Wang, H. Li, J. Xie, Z. Guo, T.-C. Lau and Y. Liu, Dual Pathways in Catalytic Ammonia Oxidation by a Ruthenium Complex Bearing a Tetradentate Bipyridine-Bipyrazole Ligand: Isolation of a Diruthenium Intermediate with a  $\mu$ -Hexazene Derivative, *J. Am. Chem. Soc.*, 2024, **146**, 21490–21495.
- B. Yuan, G. L. Tripodi, M. T. G. M. Derks, Y. Pereverzew, S. Zhou and J. Roithová, Mapping the Catalytic Cycle of Ru-Catalyzed Ammonia Oxidation, *Angew. Chem., Int. Ed.*, 2025, **64**, e202501617.
- (a) G. Chen, P. He, C. Liu, X.-F. Mo, J.-J. Wei, Z.-W. Chen, T. Cheng, L.-Z. Fu and X.-Y. Yi, Direct synthesis of hydrazine by efficient electrochemical ruthenium-catalysed ammonia oxidation, *Nat. Catal.*, 2023, **6**, 949–958; (b) C. Zhou, X. Zhang, S. Zhao, S.-D. Zhong, X.-L. Ding, S.-P. Yang, F. Pan, P. He and X.-Y. Yi, Catalytic Selective Conversion of Ammonia into Hydrazine by a RuII(trpy) Complex Bearing a Pyridylpyrrole Ligand, *ACS Catal.*, 2025, **15**, 3535–3545; (c) S. Zhao, X. Zhang, G. Chen, T. Cheng, X.-L. Ding, S.-D. Zhong, S.-P. Yang, P. He and X.-Y. Yi, Selective Electrocatalytic Oxidation of Ammonia by Ru-dpp Complexes Containing Aromatic Nitrogen Donor as Axial Ligand, *Inorg. Chem.*, 2024, **63**, 23150–23157.



- 16 (a) M. D. Zott, P. Garrido-Barros and J. C. Peters, Electrocatalytic Ammonia Oxidation Mediated by a Polypyridyl Iron Catalyst, *ACS Catal.*, 2019, **9**, 10101–10108; (b) M. D. Zott and J. C. Peters, Enhanced Ammonia Oxidation Catalysis by a Low-Spin Iron Complex Featuring cis Coordination Sites, *J. Am. Chem. Soc.*, 2021, **143**, 7612–7616; (c) M. D. Zott and J. C. Peters, Improving Molecular Iron Ammonia Oxidation Electrocatalysts via Substituent Effects that Modulate Standard Potential and Stability, *ACS Catal.*, 2023, **13**, 14052–14057.
- 17 Y. Li, J.-Y. Chen, Q. Miao, X. Yu, L. Feng, R.-Z. Liao, S. Ye, C.-H. Tung and W. Wang, A Parent Iron Amido Complex in Catalysis of Ammonia Oxidation, *J. Am. Chem. Soc.*, 2022, **144**, 4365–4275.
- 18 L. Liu, S. I. Johnson, A. M. Appel and R. M. Bullock, Oxidation of Ammonia Catalyzed by a Molecular Iron Complex: Translating Chemical Catalysis to Mediated Electrocatalysis, *Angew. Chem., Int. Ed.*, 2024, **63**, e202402635.
- 19 M. E. Ahmed, R. J. Staples, T. R. Cundari and T. H. Warren, Electrocatalytic Ammonia Oxidation by Pyridyl-Substituted Ferrocenes, *J. Am. Chem. Soc.*, 2025, **147**, 6514–6522.
- 20 (a) M. E. Ahmed, M. Raghibi Boroujeni, P. Ghosh, C. Greene, S. Kundu, J. A. Bertke and T. H. Warren, Electrocatalytic Ammonia Oxidation by a Low-Coordinate Copper Complex, *J. Am. Chem. Soc.*, 2022, **144**, 21136–21145; (b) H. Y. Liu, H. M. C. Lant, J. L. Troiano, G. Hu, B. Q. Mercado, R. H. Crabtree and G. W. Brudvig, Electrocatalytic, Homogeneous Ammonia Oxidation in Water to Nitrate and Nitrite with a Copper Complex, *J. Am. Chem. Soc.*, 2022, **144**, 8449–8453.
- 21 (a) D. N. Stephens, R. K. Szilagyi, P. N. Roehling, N. Arulsamy and M. T. Mock, Catalytic Ammonia Oxidation to Dinitrogen by a Nickel Complex, *Angew. Chem., Int. Ed.*, 2023, **62**, e202213462; (b) N. X. Gu, P. H. Oyala and J. C. Peters, Hydrazine Formation via Coupling of a Nickel(III)-NH<sub>2</sub> radical, *Angew. Chem., Int. Ed.*, 2021, **60**, 4009–4013.
- 22 H. Toda, K. Kuroki, R. Kanega, S. Kuriyama, K. Nakajima, Y. Himeda, K. Sakata and Y. Nishibayashi, Manganese-Catalyzed Ammonia Oxidation into Dinitrogen under Chemical or Electrochemical Conditions, *ChemPlusChem*, 2021, **86**, 1511–1516.
- 23 J. N. McPherson, B. Das and S. B. Colbran, Tridentate pyridine–pyrrolide chelate ligands: An under-appreciated ligand set with an immensely promising coordination chemistry, *Coord. Chem. Rev.*, 2018, **375**, 285–332.
- 24 G. Chen, X. L. Ding, P. He, T. Cheng, Y. Chen, J. Lin, X. Zhang, S. Zhao, N. Qiao and X.-Y. Yi, Understanding the factors governing the ammonia oxidation reaction by mononuclear ruthenium complex, *Chem. Sci.*, 2025, **16**, 7573–7578.
- 25 P. Štěpnička, J. Ludvík, J. Canivet and G. Süß-Fink, Relating catalytic activity and electrochemical properties: The Case of Arene-ruthenium Phenanthroline Complexes Catalytically Active in Transfer Hydrogenation, *Inorg. Chim. Acta*, 2006, **359**, 2369–2374.
- 26 J. P. da Silva, O. M. Fuganti, G. Kramer, G. Facchin, L. E. N. Aquino, J. Ellena, D. F. Back, A. C. S. Gondim, E. H. S. Sousa, L. G. F. Lopes, S. Machado, I. D. L. Guimarães, K. Wohnrath and M. P. de Araujo, Electrochemical, Mechanistic, and DFT Studies of Amine Derived Diphosphines Containing Ru(ii)-cymene Complexes with Potent in vitro Cytotoxic Activity Against HeLa and Triple-negative Breast Cancer Cells MDA-MB-231, *Dalton Trans.*, 2020, **49**, 16498–16514.
- 27 A. J. Bard, L. R. Faulkner and H. S. White, *Electrochemical Methods: Fundamentals and Applications*, 2022, p. 248.
- 28 G. W. Watt and J. D. Chrisp, Spectrophotometric Method for Determination of Hydrazine, *Anal. Chem.*, 1952, **24**, 2006–2008.
- 29 H. Y. Liu, H. M. C. Lant, J. L. Troiano, G. Hu, B. Q. Mercado, R. H. Crabtree and G. W. Brudvig, Electrocatalytic, Homogeneous Ammonia Oxidation in Water to Nitrate and Nitrite with a Copper Complex, *J. Am. Soc. Chem.*, 2022, **144**, 8449–8453.
- 30 Q. Chen, J. Liang, L. Yue, Y. Luo, Q. Liu, N. Li, A. A. Alshehri, T. Li, H. Guo and X. Sun, CoO Nanoparticle Decorated N-doped Carbon Nanotubes: a High-efficiency Catalyst for Nitrate Reduction to Ammonia, *Chem. Commun.*, 2022, **58**, 5901–5904.
- 31 (a) CCDC 2320736: Experimental Crystal Structure Determination, 2026, DOI: [10.5517/ccdc.csd.cc2hwxgs](https://doi.org/10.5517/ccdc.csd.cc2hwxgs); (b) CCDC 2324232: Experimental Crystal Structure Determination, 2026, DOI: [10.5517/ccdc.csd.cc2j0k7c](https://doi.org/10.5517/ccdc.csd.cc2j0k7c); (c) CCDC 2321021: Experimental Crystal Structure Determination, 2026, DOI: [10.5517/ccdc.csd.cc2hx6n9](https://doi.org/10.5517/ccdc.csd.cc2hx6n9); (d) CCDC 2321506: Experimental Crystal Structure Determination, 2026, DOI: [10.5517/ccdc.csd.cc2hxq9g](https://doi.org/10.5517/ccdc.csd.cc2hxq9g); (e) CCDC 2427138: Experimental Crystal Structure Determination, 2026, DOI: [10.5517/ccdc.csd.cc2mgmsj](https://doi.org/10.5517/ccdc.csd.cc2mgmsj).

